RSC Advances

PAPER

View Article Online
View Journal | View Issue

Cite this: *RSC Adv.*, 2026, **16**, 22498

Zirconium dioxide-decorated MWCNTs (ZrO_2@MWCNTs) nanocomposite as a high-performance electrochemical sensing platform for psychotropic drug analysis

Dalia A. Aboarayes,[a] Hend S. Magar, *[b] Hassan A. M. Hendawy[c] and Rabeay Y. A. Hassan *[a]

Psychotropic medications are widely prescribed for the treatment and management of various psychiatric disorders. However, several of these medications, including carbamazepine (CBZ) and quetiapine (QTP), are associated with significant risks of drug–drug interactions and exhibit narrow therapeutic indices. Consequently, the rapid, sensitive, and selective detection of CBZ and QTP is of critical importance for accurate therapeutic drug monitoring, mitigation of adverse interactions, and optimization of clinical outcomes in psychiatric care. In this regard, a highly sensitive and selective electrochemical sensing platform was developed for the determination of CBZ and QTP based on electrodes modified with zirconium oxide nanoparticle/multi-walled carbon nanotube nanocomposites (ZrO_2@MWCNTs). The electrochemical behaviors of both target analytes were comprehensively characterized using cyclic voltammetry (CV), linear sweep voltammetry (LSV), differential pulse voltammetry (DPV), and electrochemical impedance spectroscopy (EIS). The nanocomposite-modified electrodes exhibited pronounced electrocatalytic activity toward the oxidation of CBZ and QTP, as evidenced by a substantial enhancement in the oxidation peak currents and a marked decrease in their redox potentials. Under optimized experimental conditions, the proposed sensing system demonstrated outstanding analytical performance, achieving limits of detection of 0.01 μM and 0.025 μM for CBZ and QTP, respectively, along with wide linear dynamic ranges spanning 0.05–4022 μM for CBZ and 0.08–4022 μM for QTP. Moreover, the platform displayed excellent selectivity, reproducibility, and reliability and was successfully applied to the quantification of CBZ and QTP in commercial pharmaceutical formulations. The developed ZrO_2@MWCNTs-based electrochemical sensing platform represents a rapid, cost-effective, and efficient approach for psychotropic drug monitoring, with considerable potential for future implementation in pharmaceutical analysis and point-of-care testing (POCT) applications.

Received 3rd March 2026
Accepted 7th April 2026

DOI: 10.1039/d6ra01821a

rsc.li/rsc-advances

Introduction

Carbamazepine (CBZ), an iminostilbene derivative, is a first-generation antiepileptic drug that reduces irregular electrical activity in the brain. It is widely prescribed for the treatment of seizure disorders, bipolar disorder, trigeminal neuralgia, glossopharyngeal neuralgia, schizophrenia, neuromyotonia, and post-traumatic stress disorder.[1–5] However, the clinical use of CBZ is limited due to its narrow therapeutic index (NTI), as the effective plasma concentration (20–50 μM) lies very close to the range associated with its adverse or severe effects (>50 μM).[6,7]

In addition, CBZ exhibits complex drug–drug interactions (DDIs). As CBZ is a strong enzymatic inducer, it enhances the activity of hepatic cytochrome P450 enzymes (targeting CYP3A4 and CYP2B6), leading to the increased metabolism of various drugs. Conversely, CBZ metabolism is influenced by CYP inhibitors and inducers, which can result in abnormally high or low serum CBZ levels.[8]

In addition, the CBZ serum concentrations may vary with factors such as patient age, comorbidities, and dietary habits. This inter-individual variability produces a non-linear relationship between dose and plasma concentration, making therapeutic drug monitoring (TDM) essential for effective and safe therapy. TDM is particularly recommended in cases of potential DDIs, toxicity risks, or drugs exhibiting nonlinear pharmacokinetics, all of which apply to CBZ.[9]

Another notable antipsychotic medication is quetiapine (QTP), a dibenzothiazepine derivative classified as an atypical

[a]*Biosensors Research Lab, Zewail City of Science and Technology, 6th October City, Giza 12578, Egypt. E-mail: ryounes@zewailcity.edu.eg; Tel: +201129216152*
[b]*Applied Organic Chemistry Department, National Research Centre (NRC), Dokki, Giza 12622, Egypt*
[c]*National Organization for Drug Control and Research (NODCAR), P.O. Box 29, Giza, Egypt*

antipsychotic agent. It has a wide range of psychiatric applications, including the treatment of schizophrenia, bipolar disorder, obsessive-compulsive disorder, insomnia, depressive and anxiety disorders, substance abuse, dementia, and parkinsonism.

Similarly, quetiapine undergoes extensive hepatic metabolism predominantly mediated by the cytochrome P450 isoenzyme CYP3A4. Consequently, dose adjustment is necessary in patients with impaired liver function to maintain therapeutic plasma concentrations and prevent adverse reactions. Furthermore, QTP demonstrates significant drug–drug interactions with CYP3A4 modulators. Co-administration with CYP3A4 inhibitors, such as erythromycin, can suppress QTP metabolism, leading to elevated serum levels and an increased risk of toxicity or even fatal outcomes.[10]

Conversely, CYP3A4 inducers, like carbamazepine, accelerate the QTP metabolism, potentially resulting in subtherapeutic concentrations and reduced clinical efficacy.

Hence, rapid and selective detection of carbamazepine and quetiapine is critically important for ensuring accurate therapeutic drug monitoring, minimizing adverse drug interactions, and supporting the effective clinical management of psychiatric disorders. In this regard, numerous analytical techniques have been developed for the quantification of both analytes, including high-performance liquid chromatography (HPLC) coupled with mass spectrometry, liquid chromatography-tandem mass spectrometry (LC-MS/MS),[11,12] ultra-performance liquid chromatography combined with tandem mass spectrometry (UPLC-MS/MS), high-performance thin-layer chromatography (HPTLC), spectrophotometry,[13] chemiluminescence, capillary zone electrophoresis, and gas chromatography-mass spectrometry (GC-MS).[14]

Although these conventional analytical techniques provide accurate quantification, they often require sophisticated instrumentation, highly skilled personnel, invasive and time-consuming sampling procedures, labour-intensive sample preparation, and the use of environmentally hazardous solvents. Additionally, the lag between sample collection and result acquisition may delay clinical decision making, increasing the risk of adverse effects and contributing to patient non-adherence, an especially serious concern in psychiatric treatment.

To overcome these analytical limitations, increasing attention has been directed toward the development of innovative analytical approaches for the determination of CBZ and QTP in pharmaceutical formulations and biological matrices. These advancements are essential for applications in quality control, clinical monitoring, and forensic toxicology. Among these emerging methods, electrochemical techniques have gained prominence as powerful alternatives to conventional analytical procedures owing to their numerous advantages, including operational simplicity, cost-effectiveness, high sensitivity and specificity, rapid response, portability, minimal reagent consumption, and outstanding selectivity.[15,16]

The analytical performance of an electrochemical sensing platform is fundamentally dictated by the intrinsic physicochemical properties of the working-electrode interface, including mass transport processes, electron-transfer kinetics, and thermodynamic parameters that govern redox behavior.[17] These factors collectively determine the efficiency of the analyte redox reaction(s), the rate and reversibility of the interfacial electron transfer, and the reproducibility of the measured electrochemical signals. In this context, the strategic incorporation of nanostructured materials onto the electrode surface has emerged as a highly effective approach for enhancing sensor performance.[18,19] These modifications significantly increase the effective surface area, promote faster electron-transfer kinetics, and provide additional catalytic sites, thereby improving both the sensitivity and selectivity towards the target analyte(s).[20]

Consequently, nanomaterial-modified electrodes enable more accurate, robust, and reliable detection of multiple target analytes across a broad concentration range, extending the practical applicability of electrochemical methods for pharmaceutical, clinical, and environmental analyses.[21,22]

Among the various nanomaterials explored for electrochemical sensing, multi-walled carbon nanotubes (MWCNTs) have garnered significant interest due to their exceptional physicochemical properties. Their tabular nanostructure offers a large effective surface area, facilitates efficient mass transfer, and promotes catalytic activity within a confined microenvironment.[23] Furthermore, MWCNTs exhibit remarkable mechanical strength, superior electrical conductivity, high chemical stability, and a substantial specific surface area; these characteristics make them ideal candidates for electrode surface modification.[21] They also minimize the redox overpotential and enhance electron transfer, leading to more reversible and well-defined voltammetric responses compared to conventional macroelectrodes.

Moreover, a wide range of nanocomposites, comprising MWCNTs integrated with single or hybrid metal and/or metal-oxide nanostructures, such as zirconium dioxide (ZrO_2), selenium oxide, or bimetallic manganese/copper oxides, has been increasingly utilized to enhance electrochemical sensor performance.[24,25] These nanocomposites not only provided a high surface-to-volume ratio for efficient biomolecule immobilization but also promoted rapid electron-transfer kinetics and catalytic activity at the electrode interface. Consequently, the incorporation of such nanostructured hybrids significantly improves the sensitivity, selectivity, and overall analytical reliability of electrochemical detection platforms.[26–28]

In this study, a sensitive and selective electrochemical assay was developed using a ZrO_2@MWCNTs nanocomposite-modified glassy carbon electrode (GCE) to determine CBZ and QTP. The modified electrode was thoroughly characterized under optimized experimental conditions using cyclic voltammetry, linear sweep voltammetry, differential pulse voltammetry, and electrochemical impedance spectroscopy.

Materials and methods

Reagents and preparation of solutions

MWCNTs, PBS, potassium ferrocyanide ($K_4Fe(CN)_6$), potassium chloride (KCl), dimethyl sulfoxide (DMSO), isopropyl alcohol,

acetic acid, hydrochloric acid, and phosphoric acid were supplied by Piochem, Egypt. Potassium ferricyanide ($K_3Fe(CN)_6$) was obtained from Loba Chemie, India. Sodium hydroxide was obtained from Power Chemical, Egypt. Boric acid was supplied by British Drug Houses Ltd, England. Standard materials for quetiapine fumarate (QTPF) and CBZ were provided by the National Organization for Drug Control and Research (NODCAR), Egypt. Sodium acetate was obtained from Rankem, India. Tris was obtained from Molekula, UK. Citric acid anhydrous was obtained from Fisher Scientific, USA. Sodium citrate dihydrate, disodium phosphate, and aluminium oxide polishing powder were procured from Sigma-Aldrich.

Supporting electrolytes and buffer preparation

Solutions of universal Britton–Robinson buffer (BRB) were prepared by dissolving 10 mM of each of the three different triprotic acids (citric acid, boric acid, and phosphoric acid) in a definite volume of double-distilled water. Acetate buffer was prepared by mixing 10 mM acetic acid and 10 mM sodium acetate, followed by dilution with distilled water to the desired volume. Citrate-phosphate buffer was prepared by combining 10 mM citric acid and 10 mM disodium hydrogen phosphate (Na_2HPO_4) and diluting with double-distilled water to the desired volume. Phosphate-buffered saline (PBS) was prepared by dissolving commercially available PBS tablets in an appropriate volume of distilled water, followed by sonication until a clear solution was obtained. Tris–HCl buffer was prepared by mixing 10 mM Tris-base with 10 mM hydrochloric acid (HCl), followed by dilution with distilled water. The pH values of all buffers were adjusted as required using standardized HCl or NaOH solutions. All reagents were used as received without further purification, and all buffer preparations and experiments were performed at room temperature (25 ± 2.0 °C).

Modification of GCE with the ZrO_2@MWCNTs nanocomposite

For electrode surface modification with the nanomaterials, the GCE surface was first polished with alumina powder (Al_2O_3), rinsed with ethanol, and ultrasonicated twice in distilled water for 5.0 minutes to remove residual polishing particles. Subsequently, the GCEs were individually coated with several metal oxides (5.0 mg mL^{-1} of each metal oxide dispersed in double-distilled water) that were sonicated for 30 minutes to obtain a homogeneous suspension. Subsequently, 20 μL of the resulting suspension was drop-cast onto the pre-cleaned GCE surface and dried at room temperature.

To prepare the ZrO_2@MWCNTs nanocomposite, 2.5 mg of zirconium dioxide (ZrO_2) and 2.5 mg of multi-walled carbon nanotubes (MWCNTs) were mixed in 1.0 mL of double-distilled water and ultrasonicated for 30 minutes to form a uniform dispersion of the nanocomposite. Then, 20 μL of the composite suspension was thoroughly drop-cast onto the GCE surface and allowed to dry at room temperature.

Subsequently, the optimization of the ZrO_2 ratio was further investigated. Three weight ratios were tested: (i) 1.0 mg ZrO_2 with 4.0 mg MWCNTs, (ii) 4.0 mg ZrO_2 with 1.0 mg MWCNTs, and (iii) 2.5 mg ZrO_2 with 2.5 mg MWCNTs. Each mixture was dispersed in 1.0 mL of deionized water and sonicated for 30 minutes, and 20 μL of each suspension was drop-cast onto the GCE surface, followed by drying at room temperature.

Electrochemical characterization of the modified electrodes was conducted in triplicate using cyclic voltammetry and electrochemical impedance spectroscopy. Measurements were performed in a 5.0 mM solution of potassium ferricyanide/potassium ferrocyanide prepared in 0.1 M potassium chloride (KCl) as the supporting electrolyte.

Electrochemical measurements

Electrochemical analyses, including cyclic voltammetry (CV) and linear sweep voltammetry (LSV), were performed using a Gamry potentiostat (version 6.33) and a Corrtest CS350H electrochemical workstation. Differential pulse voltammetry (DPV) and electrochemical impedance spectroscopy (EIS) measurements were conducted using a PalmSens potentiostat (Randhoeve, Netherlands). All experiments were carried out using a conventional three-electrode cell configuration comprising a glassy carbon working electrode (GCE; disk diameter 3.0 mm, length 80 mm; Corrtest Instruments, China), a silver wire reference electrode, and a silver wire counter electrode.

EIS measurements were performed at open-circuit potential (OCP) with an AC perturbation amplitude of 10 mV over a frequency ranging from 10 kHz to 0.1 Hz. The obtained Nyquist plots were analyzed by fitting to an appropriate equivalent circuit model for quantitative interpretation. Voltammetric measurements were conducted by sweeping the potential from −0.4 V to +0.9 V *vs.* the Ag/AgCl at a scan rate of 50 mV s^{-1}. All electrochemical measurements were performed at room temperature (25 ± 2.0 °C).

Physical characterization of the ZrO_2@MWCNTs nanocomposite

The phase structure and crystallinity of the synthesized ZrO_2@MWCNTs nanocomposite were analyzed using X-ray powder diffraction (XRD) with a Bruker D8 diffractometer. Morphological features were examined by transmission electron microscopy (TEM) using a JEOL JEM-1230 instrument. Fourier transform infrared spectroscopy (FTIR) was performed using a Thermo Fisher iQ-10 spectrometer (USA) to confirm the chemical composition, surface functionalities, and bonding configurations of the nanocomposite.

Assay optimization

Optimization of the electrochemical response for carbamazepine and quetiapine was performed using the ZrO_2@MWCNTs-modified electrode. The influence of different supporting electrolytes (including PBS, BRB, acetate, citrate-phosphate, and Tris–HCl buffers) was investigated at pH 7.0. Subsequently, the effect of pH on the electrochemical response was further evaluated using PBS in the pH range of 3.0–9.0. The optimal oxidation peak current was obtained at pH 7.0. Additional

studies were conducted to assess the effects of scan rate (50–300 mV s^{-1}) and deposition potential (0.0–0.5 V).

Interference study

The selectivity of the developed electrochemical sensor toward CBZ and QTP was systematically evaluated through interference studies involving both common pharmaceutical excipients and endogenous electroactive species. All measurements were performed under previously optimized experimental conditions using linear sweep voltammetry (LSV).

To assess the effect of pharmaceutical additives, a series of commonly used excipients were investigated, including silica colloidal anhydrous, ethylcellulose aqueous dispersion, microcrystalline cellulose, polyacrylate, magnesium stearate, sodium carmellose, hypromellose, macroglycerol hydroxystearate, titanium dioxide, povidone, sodium starch glycolate Type A, lactose monohydrate, macrogol, ferric oxide, iron oxide yellow (E172), iron oxide red (E172), and crospovidone. Each excipient was individually introduced into an electrochemical cell containing standard solutions of CBZ or QTP. The corresponding voltammetric responses were recorded and compared with those obtained in the absence of interfering species.

To evaluate performance in the presence of biologically relevant interferents, ascorbic acid, uric acid, and dopamine were selected as representative endogenous electroactive compounds. These species were tested both individually and in combination with CBZ and QTP. LSV measurements were conducted to monitor any changes in peak current, peak potential, or signal shape. Mixed solutions containing the target analytes and interfering species were prepared to simulate competitive electrochemical environments.

All experiments were carried out using a ZrO_2@MWCNTs-modified glassy carbon electrode (GCE). The voltammetric profiles were analyzed to determine the extent of the signal overlap, peak resolution, and potential redox interference. The reproducibility and stability of the sensor response were also monitored throughout the interference assessments to ensure reliability under complex matrix conditions.

CBZ and QTP analyses of pharmaceutical formulations

The ZrO_2@MWCNTs@GCE electrode was utilized for the voltammetric analysis of CBZ and QTP in real pharmaceutical formulations. Tegretol® CR 200 mg and Tegretol® CR 400 mg (Novartis Pharma, Egypt) were used as CBZ sources, while Seroquel® 25 mg (AstraZeneca, China) and Quitapex® 25 mg (Apex Pharma, Egypt) were used for QTP analysis.

For CBZ analysis, a single tablet of Tegretol® CR 200 mg was dissolved in 10 mL of DMSO, and Tegretol® CR 400 mg was dissolved in 20 mL of DMSO. Each solution was sonicated until homogeneous. From each, 500 μL was diluted with 500 μL PBS; then, 500 μL of this mixture was diluted with 4.5 mL PBS. These solutions were used at varying concentrations for the CBZ electrochemical analysis by LSV.

For QTP, individual Seroquel® 25 mg and Quitapex® 25 mg tablets were dissolved in 676 μL of DMSO and sonicated until homogeneous. Then, 500 μL of each solution was diluted with 4.5 mL of PBS. The prepared solutions were used at different concentrations to study QTP electrochemical behavior using LSV.

Results and discussion

Structural and morphological characterization of the ZrO_2@MWCNTs nanocomposite

The structural and morphological features of the synthesized ZrO_2@MWCNTs nanocomposite were comprehensively analyzed using FTIR, XRD, and TEM techniques. Fourier-transform infrared (FTIR) spectroscopy was employed to identify the surface functional groups and bonding interactions in pure solid powder of ZrO_2, pristine MWCNTs, and the ZrO_2@MWCNTs composite (Fig. 1A). The FTIR spectrum of ZrO_2 exhibited a broad absorption band between 400 and 700 cm^{-1}, which corresponded to the Zr–O stretching vibration, confirming the presence of zirconium oxide. The spectrum of MWCNTs displayed characteristic bands at approximately 3430 cm^{-1} (O–H stretching), 2920 cm^{-1} (C–H stretching), 1630 cm^{-1} (C=C stretching of the graphitic backbone), and 1100 cm^{-1} (C–O stretching), indicating partial surface oxidation and the existence of oxygen-containing functional groups.

For the ZrO_2@MWCNTs nanocomposite, the characteristic Zr–O stretching vibration was clearly preserved, confirming the structural integrity of the zirconia phase after composite formation. Notably, a reduction in the intensity of the O–H and C–O vibrational bands was observed, which could be attributed to the involvement of oxygen-containing functional groups on the MWCNTs surface in interfacial interactions with ZrO_2 nanoparticles. This attenuation suggests the partial modification of surface hydroxyl and carboxyl groups during the anchoring process. Furthermore, slight shifts in the C=C stretching band of the graphitic framework and in the Zr–O stretching region were detected, indicating electronic perturbation and the establishment of strong interfacial coupling between ZrO_2 and the carbon nanotube network. These spectral changes are consistent with the formation of chemical bonding or robust coordination interactions rather than simple physical adsorption. These spectroscopic findings pointed to the homogeneous distribution of ZrO_2 nanoparticles onto the MWCNTs surface, resulting in a stable and well-integrated hybrid nanostructure with enhanced interfacial compatibility.

Consequently, the X-ray diffraction (XRD) patterns were recorded to determine the crystalline phases and structural integrity of ZrO_2, MWCNTs, and their composites (Fig. 1B). Pure ZrO_2 displayed distinct diffraction peaks at $2\theta \approx 28.2°$, 31.5°, 34.3°, and 50.1°, which are indexed to the (−111), (111), (002), and (112) planes, respectively, confirming the monoclinic phase (JCPDS No. 37-1484). The MWCNTs exhibited a broad peak centered on $2\theta \approx 26°$, corresponding to the (002) plane of graphitic carbon, which reflects their semi-crystalline nature. In the XRD pattern of the ZrO_2@MWCNTs composite, diffraction peaks from both ZrO_2 and MWCNTs were present, confirming the coexistence of both components. The slight reduction and broadening of the (002) peak intensity of MWCNTs suggested a strong interaction between ZrO_2 nanoparticles and the

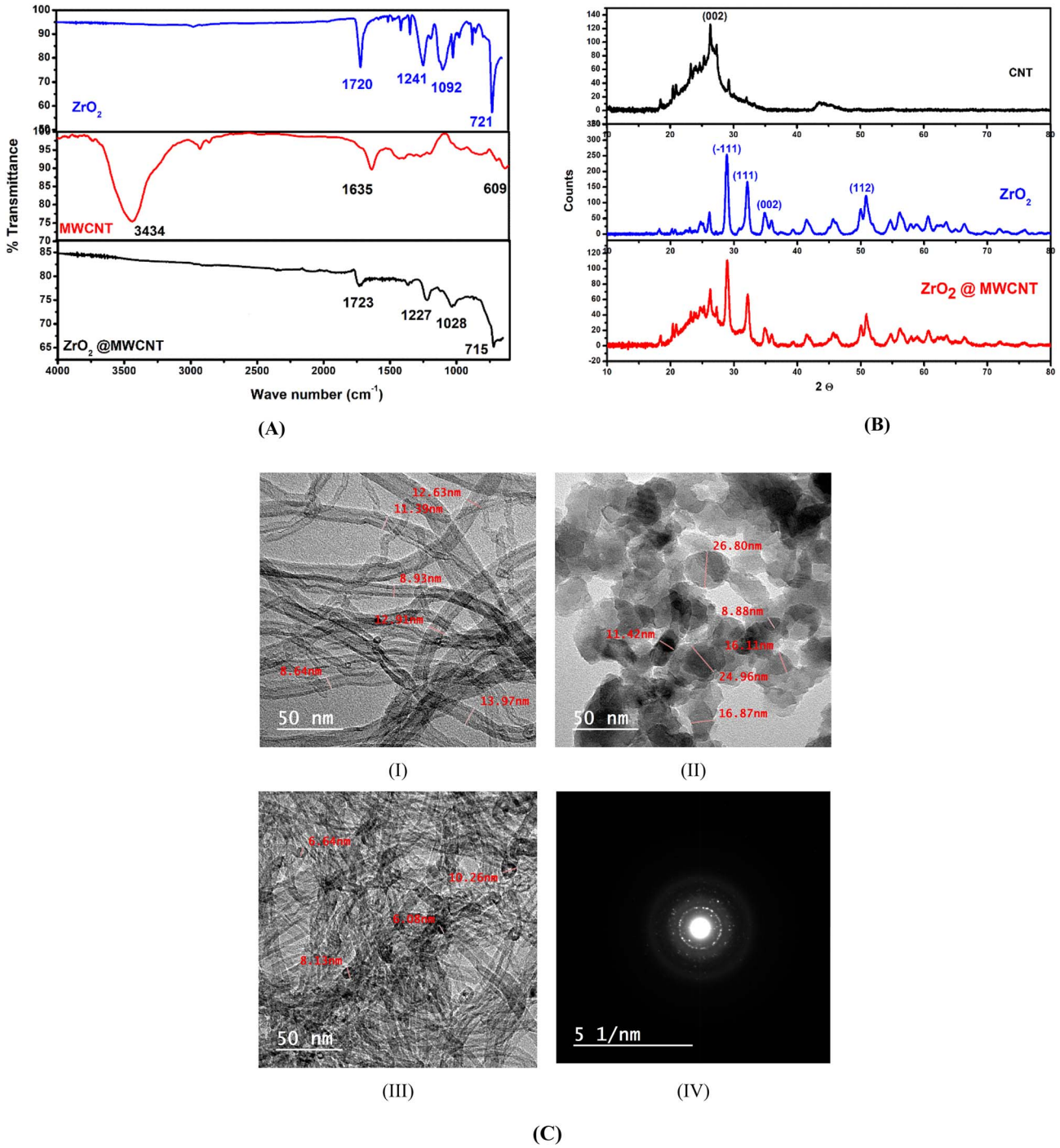

Fig. 1 (A) FTIR spectra recorded from the MWCNTs, ZrO_2 and ZrO_2@MWCNTs nanocomposite. (B) X-ray diffraction (XRD) patterns of pure ZrO_2, MWCNTs, and the ZrO_2@MWCNTs composite. (C) TEM images of the (I) MWCNTs, (II) ZrO_2, and (III) ZrO_2@MWCNTs nanocomposite. (IV) The corresponding diffraction pattern of ZrO_2@MWCNTs.

nanotube surfaces possibly due to partial surface coverage or strain effects during decoration.

Furthermore, 2D imaging using transmission electron microscopy (TEM) was utilized to observe the morphology, particle size, and distribution of ZrO_2 nanoparticles on the MWCNTs (Fig. 1C). TEM images of pure ZrO_2 revealed quasi-spherical nanoparticles with an average diameter of 10–20 nm, exhibiting mild agglomeration due to high surface energy. The MWCNTs showed characteristic multi-walled tubular structures with outer diameters ranging from 20 to 40 nm and hollow interiors, confirming their graphitic cylindrical morphology. Furthermore, the TEM images of the ZrO_2@MWCNTs composite displayed uniformly dispersed ZrO_2 nanoparticles anchored along the outer walls of the nanotubes, with minimal aggregation. The intimate interfacial contact and homogeneous decoration indicated strong interactions

between the ZrO_2 nanoparticles and the MWCNTs surfaces. Furthermore, no observable damage or deformation of the nanotube structure was detected, suggesting that the integration route effectively preserved the structural integrity of the MWCNTs. The high interfacial contact area between ZrO_2 and MWCNTs is expected to promote efficient charge transfer, a desirable property for catalytic and electrochemical sensing applications.

Electrochemical screening of nanomaterials

To develop a highly sensitive and reliable electrochemical platform for the rapid detection of the target pharmaceutical analytes, systematic electrochemical characterization and screening of several nanomaterials were performed using the CV and EIS, respectively. All nanostructure-electrodes were evaluated using the $K_3[Fe(CN)_6]/K_4[Fe(CN)_6]$ (5.0 mM in 0.1 M KCl) to assess electron-transfer efficiency.

As shown in Fig. 2A and summarized in Table S1, GCEs modified with various metal oxide nanostructures, including ZrO_2, La_2O_3, V_2O_5, TiO_2, Sb_2O_3, and NiO, exhibited significantly enhanced anodic peak currents compared to the bare-GCE (21.39 μA). The peak currents followed the order ZrO_2 (32.65 μA) > La_2O_3 (30.02 μA) > TiO_2 (29.78 μA) > V_2O_5 (28.32 μA) > NiO (27.69 μA) > Sb_2O_3 (14.60 μA), highlighting the added electrochemical reactivity of ZrO_2.

However, the EIS and double-layer capacitance analyses further validated these results, while the generated charge-transfer resistance (R_{ct}) for ZrO_2-modified electrodes was the lowest among all the tested nanomaterials (35.5 Ω), compared to La_2O_3 (102 Ω), TiO_2 (1210.3 Ω), V_2O_5 (2510 Ω), NiO (3248 Ω), and Sb_2O_3 (7254.3 Ω), confirming efficient electron-transfer pathways (Table S1). Collectively, these results identified ZrO_2 as the optimal metal oxide for further electrode modification.

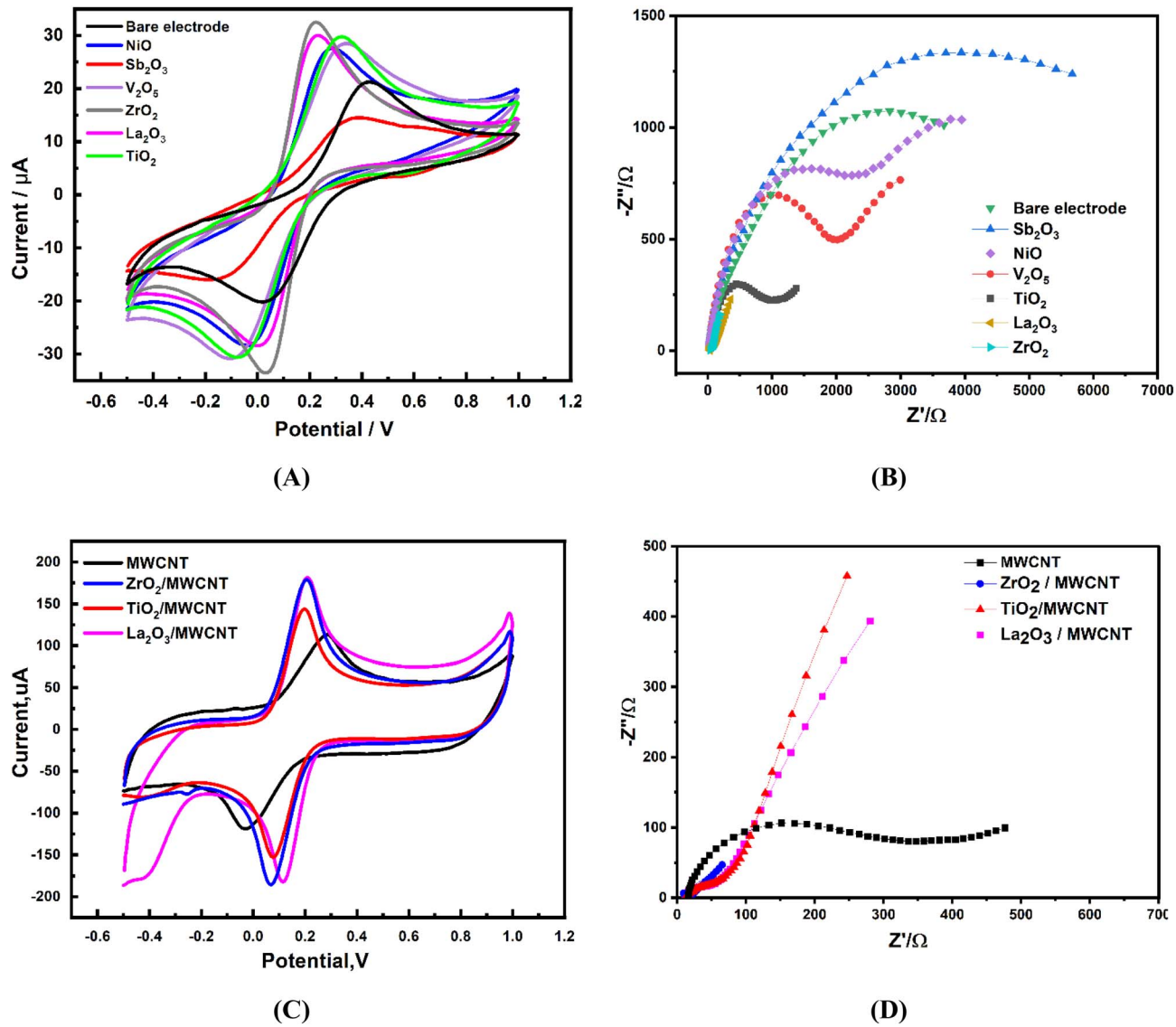

Fig. 2 (A) CV and (B) EIS of the unmodified and modified GCE with different metal oxides (NiO, Sb_2O_3, V_2O_5, ZrO_2, La_2O_3 and TiO_2). (C) CV and (D) EIS of different metal oxides@MWCNTs. Measurements were conducted in 5.0 mM $[Fe_3(CN)_6]^{3-/4-}$ with 0.1 M KCl at a scan rate of 50 mV s^{-1}.

Consequently, to enhance conductivity and electrocatalytic performance, ZrO_2 was integrated with multi-walled carbon nanotubes (MWCNTs) to form a hybrid ZrO_2@MWCNTs nanocomposite. As mentioned above, the FTIR analysis revealed the formation of a stable and well-integrated hybrid structure. Thus, the electrochemical properties of the ZrO_2@MWCNTs composite were evaluated and compared to bare GCE and individual components (ZrO_2 or MWCNTs). As a result, the hybrid nanocomposite demonstrated remarkable enhancement in voltammetric performance. The oxidation peak current increased from 21.4 μA for the bare-GCE to 188.9 μA for the ZrO_2@MWCNTs-modified electrode, representing an over eightfold increase (Fig. 2C and Tables S1 and S2).

EIS measurements revealed a dramatic decrease in the obtained R_{ct}: bare GCE 5968 Ω → MWCNTs-modified 340.2 Ω → ZrO_2@MWCNTs-modified 9.8 Ω (Fig. 2D). This significant improvement reflects the synergistic interaction between crystalline ZrO_2 nanoparticles and the highly conductive MWCNTs network, which promotes rapid electron transport and enhances electro–catalytic activity. Consequently, the ZrO_2@-MWCNTs-modified electrode provides a high-performance platform for sensitive and reproducible electrochemical detection of pharmaceutical analytes.

Electrochemically active surface area (ECSA) evaluation

The electrochemically active surface area (ECSA) of the working electrode in such electrochemical systems is a critical parameter for assessing the efficiency and catalytic performance of modified electrodes. It provides direct insight into the accessibility of electroactive sites and the extent of charge transfer between the electrode surface and redox species. In this study, the ECSA values of bare and ZrO_2@MWCNTs electrodes were determined using the CV in a 5.0 mM $[Fe_3(CN)_6]^{3-}/^{4-}$ redox probe with 0.1 M KCl as the supporting electrolyte at different scan rates (as shown in Fig. 3A and C). Accordingly, the calculation of the ECSA was carried out using the Randles–Ševčík equation,[29] which describes the relationship between the voltammetric peak current (I_p) and various system parameters for a reversible redox process at 25 °C:

$$I_p = (2.69 \times 10^5) n^{3/2} A D^{1/2} C v^{1/2}, \quad (1)$$

where (I_p) is the voltammetric peak current, (n) is the number of electrons transferred, (A) is the electroactive surface area (cm^2) of the working electrode, (D) is the diffusion coefficient of the redox species ($cm^2\ s^{-1}$), (C) is the analyte concentration (mol cm^{-3}), and (v) is the scan rate ($V\ s^{-1}$).

By plotting I_p against the square root of the scan rate ($v^{1/2}$), a linear correlation is obtained, and the slope of this line is used along with known constants to calculate the changes in ECSA.

The CV results (Fig. 3B and D) demonstrated a well-defined, linear relationship between the redox peak current and the square root of the scan rate, confirming a adsorption-controlled process at both bare and modified electrodes. The bare GCE exhibited relatively small redox peak currents, indicating a limited electroactive area and sluggish electron transfer. Upon modification with the ZrO_2@MWCNTs nanocomposite, a substantial enhancement in redox current was observed, reflecting an expanded electroactive surface and improved electron-transfer dynamics and kinetics.

This improvement can be attributed to the synergistic effects of the ZrO_2 nanoparticles and the MWCNTs framework. The high surface area and conductivity of MWCNTs provide efficient electron transport pathways, while dispersed ZrO_2 nanoparticles introduce additional active sites and promote interfacial redox interactions. Consequently, the ZrO_2@MWCNTs-modified electrode exhibited a significantly higher ECSA value of 1.026 cm^2, compared with only 0.093 cm^2 for the bare GCE, representing nearly a 10-fold enhancement. The enlarged electroactive area and improved charge transport characteristics of the ZrO_2@-MWCNTs nanocomposite play a pivotal role in enhancing its electrocatalytic performance, confirming its suitability as an efficient sensing platform for CBZ and QTP detection.

Voltammetric assay optimization for CBZ and QTP detection

Following the identification of the ZrO_2@MWCNTs nanocomposite as a highly promising sensing material, optimization studies were conducted to determine the ideal composition and experimental conditions for maximizing the electrochemical response toward the target analytes, carbamazepine (CBZ) and quetiapine (QTP).

Comparative electrochemical investigations were performed to elucidate the individual contributions of each component within the developed nanocomposite system. Measurements were carried out using the bare electrode, electrodes modified solely with MWCNTs, electrodes modified solely with ZrO_2 nanoparticles, and electrodes modified with the ZrO_2@-MWCNTs nanocomposite. The bare GCE exhibited relatively low peak currents, indicating limited electrocatalytic activity and slow electron-transfer kinetics toward the analytes. Modification with MWCNTs resulted in a marked enhancement of the electrochemical response, which is attributed to the high electrical conductivity, large specific surface area, and efficient electron-transport pathways provided by the interconnected nanotube network. Electrodes modified solely with ZrO_2 nanoparticles showed a moderate increase in the current response. Remarkably, the ZrO_2@MWCNTs-modified electrode demonstrated significantly higher peak currents and improved signal reproducibility compared with electrodes containing individual components. This enhanced performance arises from the synergistic interaction between the conductive MWCNTs framework and the catalytically active ZrO_2 nanoparticles. The MWCNTs matrix promotes rapid electron transfer and provides an expanded electroactive surface area, while uniformly distributed ZrO_2 nanoparticles introduce abundant catalytic and adsorption sites for analyte interaction. This cooperative effect substantially enhances electrocatalytic activity, sensitivity, and overall sensing performance toward CBZ and QTP.

As shown in Fig. 4A, both analytes exhibited distinct redox activity at the electrode surface. CBZ displayed a well-defined irreversible oxidation peak at approximately 1.042 V, with a peak current of 160 μA, compared with 2.0 μA at the bare electrode. QTP exhibited a prominent oxidation peak at 0.78 V,

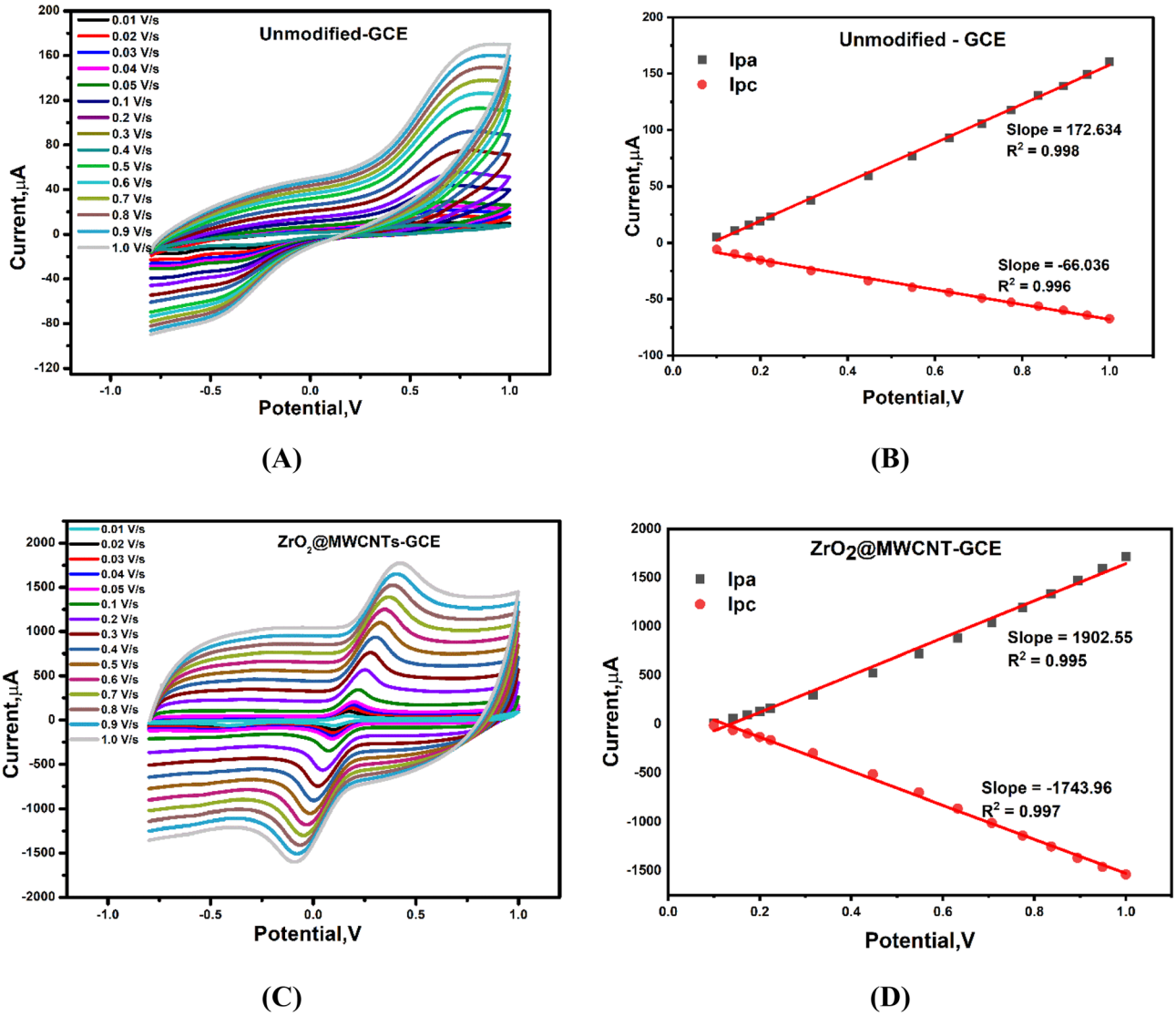

Fig. 3 (A and C) Cyclic voltammograms of bare and ZrO_2@MWCNTs-modified glassy carbon electrode (GCE) recorded in 5.0 mM $[Fe_3(CN)_6]^{3-/4-}$ with 0.1 M KCl at varying scan rates. (B and D) Corresponding linear plots of peak current (I_p) *versus* the square root of scan rate ($v^{1/2}$) are used to estimate the electrochemically active surface area (ECSA) using the Randles–Ševčík equation.

with a peak current of 38 μA. Notably, the ZrO_2@MWCNTs-modified electrodes significantly enhanced the direct electro-oxidation of both analytes, producing a pronounced increase in faradaic peak currents, as illustrated in Fig. 4A.

To optimize the ZrO_2-to-MWCNTs ratio, three weight ratios were evaluated: (i) 1.0 mg ZrO_2 with 4.0 mg MWCNTs, (ii) 4.0 mg ZrO_2 with 1.0 mg MWCNTs, and (iii) 2.5 mg ZrO_2 with 2.5 mg MWCNTs. Each mixture was dispersed in 1.0 mL of distilled water and sonicated for 30 minutes, and 20 μL of each suspension was drop-cast onto the GCE surface and dried at room temperature. Among the tested formulations, the 1 : 1 ratio produced the highest anodic peak currents, reflecting superior electron-transfer efficiency and enhanced electrocatalytic activity. This improvement is attributed to the optimal balance between the catalytic properties of ZrO_2 and the high electrical conductivity of MWCNTs, which facilitates charge transport and provides an enlarged active surface area. Higher ZrO_2 content (*e.g.*, 4 : 1 ZrO_2) led to a marked decrease in voltammetric signal likely due to the semiconducting nature of ZrO_2, which restricts electron mobility at elevated concentrations, reducing the overall electrochemical performance of the composite. Consequently, the 1 : 1 ratio was selected as the optimal composition for all subsequent electrochemical measurements.

The effect of the supporting electrolyte on the oxidation peak currents of CBZ and QTP was assessed using phosphate buffer solution (PBS), Britton–Robinson buffer (BRB), acetate buffer, citrate-phosphate buffer, and Tris buffer (Fig. 4C). Among these, PBS yielded the most pronounced and well-defined oxidation peaks for both analytes, reflecting its superior ionic conductivity, buffering capacity, and compatibility with the modified electrode surface. Therefore, PBS was chosen as the optimal supporting electrolyte.

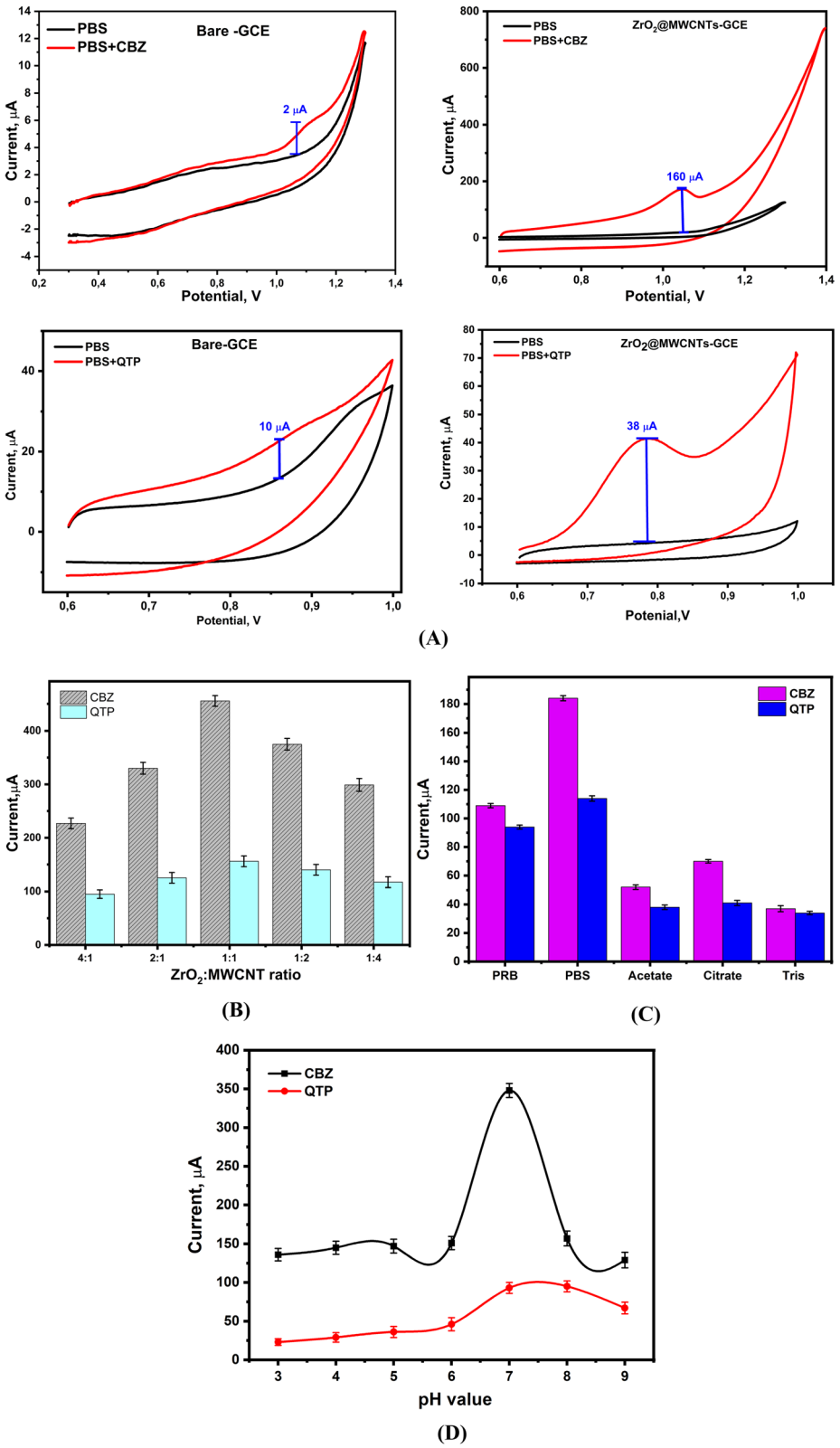

Fig. 4 (A) Cyclic voltammetric profiles of carbamazepine (CBZ) and quetiapine (QTP) recorded at the bare GCE and ZrO_2@MWCNTs-modified electrodes, illustrating the enhanced electrochemical response and catalytic activity of the nanocomposite-modified surface. (B) Effect of ZrO_2@MWCNTs nanocomposite ratio toward the oxidation peak current of CBZ and QTP. (C) Effect of electrolyte buffer type (PBS, BRB, acetate buffer, citrate phosphate buffer, and Tris-buffer) on the oxidation peak current of CBZ and QTP. (D) Effect of pH changes on the peak current of CBZ and QTP oxidation.

Subsequently, the influence of solution pH on the electrochemical behavior of CBZ and QTP was investigated in a pH range of 3.0–9.0 using PBS. As shown in Fig. 4D, maximum oxidation peak currents were observed at pH 7.0. Deviations from this pH led to notable decreases in signal intensity and stability: acidic media (pH < 6) caused degradation of the nanocomposite surface, whereas alkaline conditions (pH > 8) produced unstable and noisy voltammetric responses likely due to hydroxide formation and decreased analyte stability.

Thus, the combination of a 1 : 1 ZrO_2@MWCNTs nanocomposite and PBS at pH 7.0 was established as the optimal condition, ensuring both stability and high sensitivity for the voltammetric detection of CBZ and QTP.

Voltammetric oxidation mechanisms and electron transfer determination

The electrochemical oxidation mechanisms of the CBZ and QTP at the ZrO_2@MWCNTs-modified electrodes were systematically investigated through scan rate studies to elucidate the nature of the electron transfer process and the number of electrons involved (Fig. S1, SI). Thus, the voltammetric response of both analytes was examined over a range of scan rates (50–300 mV s^{-1}) under constant experimental conditions (Fig. S1A and B). As the scan rate increased, a proportional enhancement in the oxidation peak current (I_p) was observed, accompanied by a gradual positive shift in the peak potential (E_p) (Fig. S1C and D). The plots of I_p *versus* the square root of the scan rate ($v^{1/2}$) displayed excellent linearity (Fig. S1E and F), confirming that the irreversible molecular oxidation processes of CBZ and QTP are predominantly adsorption-controlled.

This conclusion is consistent with Laviron's theoretical model for irreversible electrochemical reactions (eqn (2)):

$$E_p = E_0^{'} + (RT/\alpha nF)\log(RTk_0/\alpha nF) + (RT/\alpha nF)\log\ v, \quad (2)$$

where ($E_0^{'}$) is the formal potential (V), (R) is the gas constant (8.314 J mol^{-1} K^{-1}), (T) is the temperature (298 K), (α) is the charge-transfer coefficient, (n) is the number of electrons transferred, and (F) is the Faraday constant (96 485 C mol^{-1}). The slope of the linear relationship between (E_p) and ($\log v$) is given by ($2.303RT/\alpha nF$), enabling the calculation of (n).

Accordingly, from the experimentally obtained slope values (0.0569 V) for CBZ and (0.032 V) for QTP, the corresponding electron transfer numbers were determined to be approximately $n \approx 1.0$ for CBZ and $n \approx 2.0$ for QTP, assuming $\alpha = 0.5$ and $\alpha = 0.373$, respectively. These results strongly support the proposed oxidation mechanisms illustrated in (Scheme S1A and B, SI).

For the CBZ, the oxidation begins with a one-electron transfer at the nitrogen center, forming a carbamazepine radical cation ($CBZ^{\bullet+}$). This reactive intermediate undergoes structural rearrangement and dimerization *via* radical coupling at the 2-position, yielding a CBZ dimer.

For the QTP, the electrooxidation proceeds through a two-electron, one-proton process at the piperazine moiety, leading to the formation of a transient tertiary ammonium radical intermediate. Subsequent deprotonation and rearrangement yield an imine product, a transformation that is irreversible due to the lack of enamine-imine interconversion.

Electrode performance and calibration curves

The ZrO_2@MWCNTs-modified electrodes exhibited broad linear response ranges for both CBZ and QTP without signal saturation (as depicted in Fig. S2A and B, SI). The calibration curves (Fig. S2C and D) revealed a dynamic linearity increase between the oxidation current and logarithm of the targeting analyte concentration ranging from 1.0×10^{-6} to 1.0×10^{-1} M, with sensitivities of 77 μA μM^{-1} for CBZ and 22.36 μA μM^{-1} for QTP, respectively.

The superior analytical performance is attributed to the synergistic properties of the nanocomposite, enlarged/expanded electroactive surface area, high electrical conductivity, and efficient electron transport pathways provided by the MWCNTs matrix combined with the catalytic functionality of ZrO_2. These characteristics collectively establish the ZrO_2@-MWCNTs-modified electrode as a robust and highly responsive platform for the electrochemical sensing of therapeutic drugs.

Consequently, the DPV and LSV techniques were employed to evaluate key analytical parameters, including selectivity, sensitivity, dynamic linear range, and detection limits of the ZrO_2/MWCNTs-modified electrodes in response to the direct oxidation of the target analytes (CBZ and QTP) in PBS. As shown in Fig. 5A, the relationship between the anodic peak current and accumulation time was studied using the proposed sensor in phosphate-buffered saline (PBS, pH 7.0) containing 300 μM each of CBZ and QTP at a scan rate of 50 mV s^{-1}. The oxidation peak current increased with increasing accumulation time up to 13 seconds and then declined. This decrease is likely due to surface saturation by CBZ or QTP. Consequently, an accumulation time of 13 seconds was selected as optimal for further experiments.

In addition, Fig. 5B presents the DPV responses of ZrO_2@-MWCNTs-modified electrodes toward a fixed concentration of CBZ in PBS (pH 7.0) at various deposition potentials ranging from 0.0 V to 0.5 V. The maximum oxidation peak current was recorded at 0.2 V, which was therefore chosen as the optimal deposition potential for subsequent measurements.

Using the DPV and LSV techniques, the electrochemical responses of CBZ and QTP were evaluated across a range of concentrations. For CBZ (Fig. 6), a linear relationship was observed between the oxidation peak current and concentration in the range of 0.08–200 μM using the DPV method and 0.08–4022 μM using LSV, with correlation coefficients (R^2) ranging from approximately 0.994 to 0.999. In the case of QTP (Fig. 7), both the DPV and LSV methods demonstrated linear behaviour over a concentration range of 0.08–4022 μM, with correlation coefficients between ~0.995 and 0.998.

The limits of detection for CBZ and QTP were determined to be 0.01 μM and 0.025 μM, respectively, which were calculated using the following equation: LOD = 3SD/slope, where SD denotes the standard deviation. These values reflect the excellent sensitivity of the developed sensor. Furthermore, when comparing the linear detection ranges and LODs of the

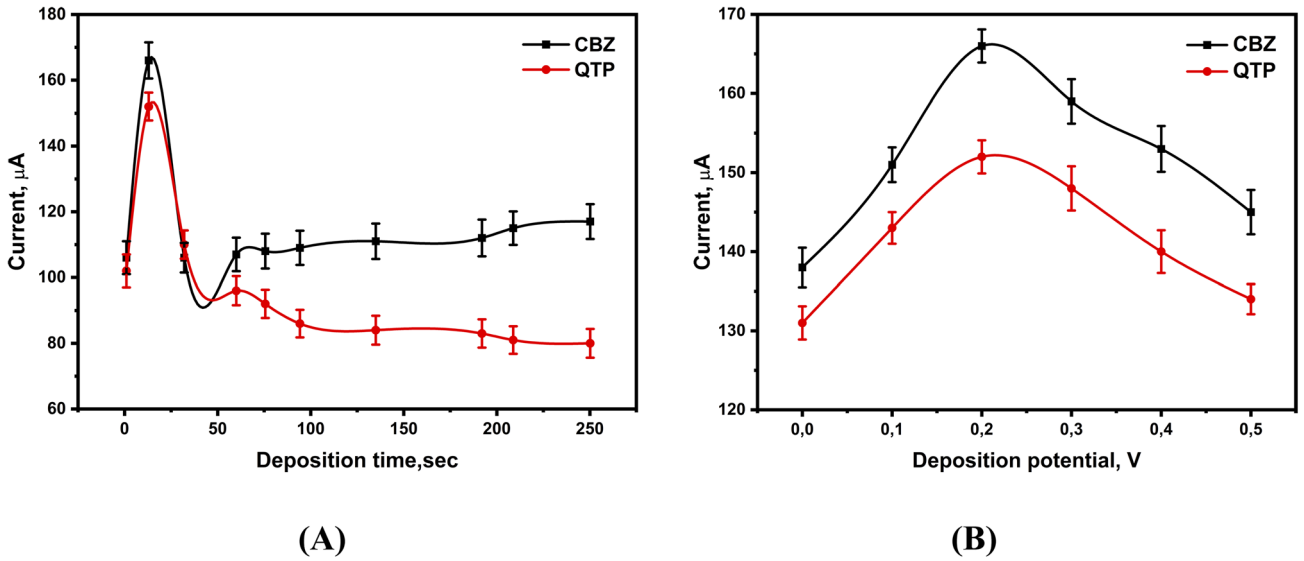

Fig. 5 (A) Effect of deposition time and (B) effect of deposition potential on CBZ and QTP oxidation peak current response.

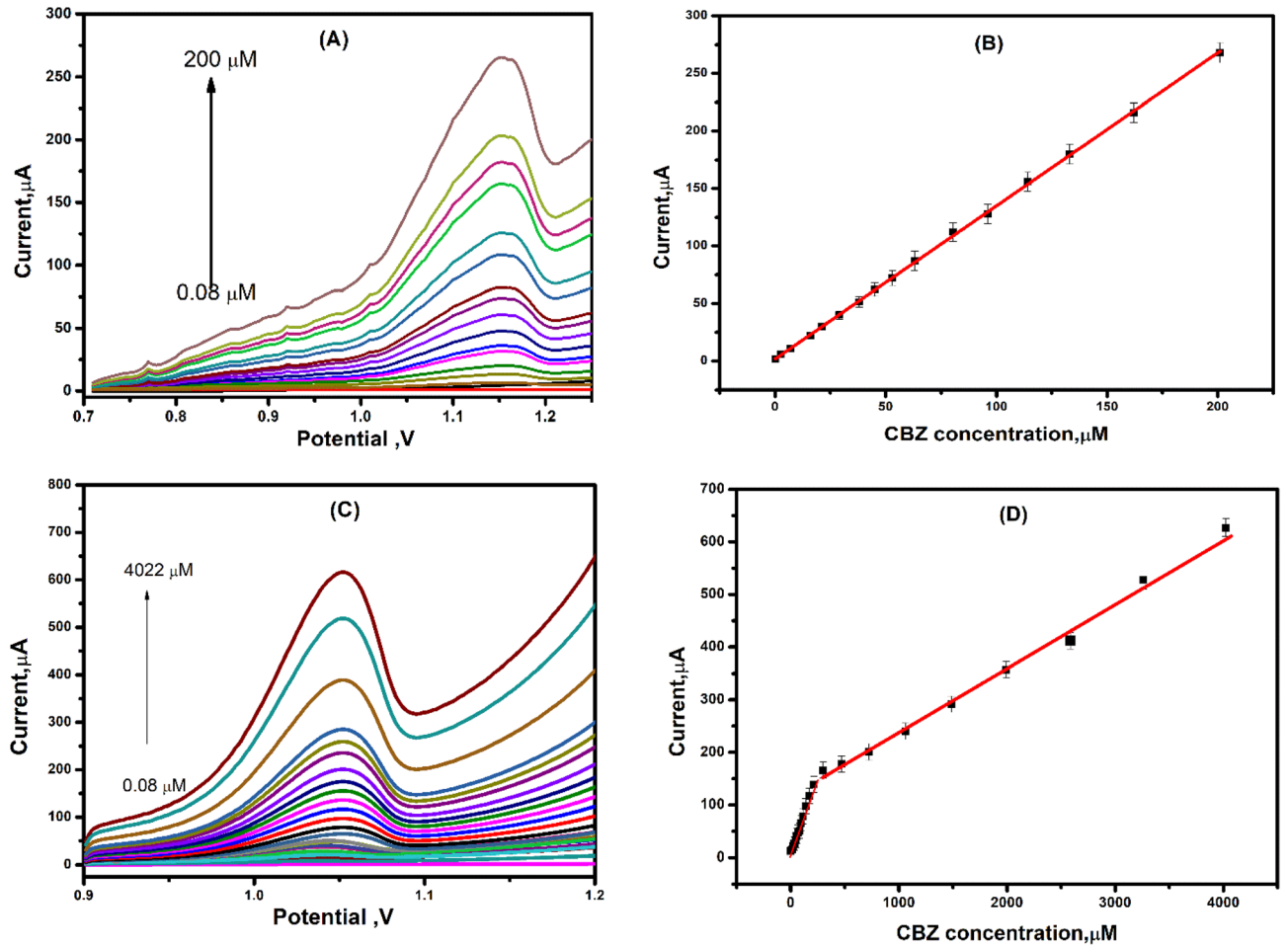

Fig. 6 (A) DPV peaks and (B) linear calibration curve for CBZ detection. (C) LSV oxidation peaks and (D) linear calibration curve for the CBZ response.

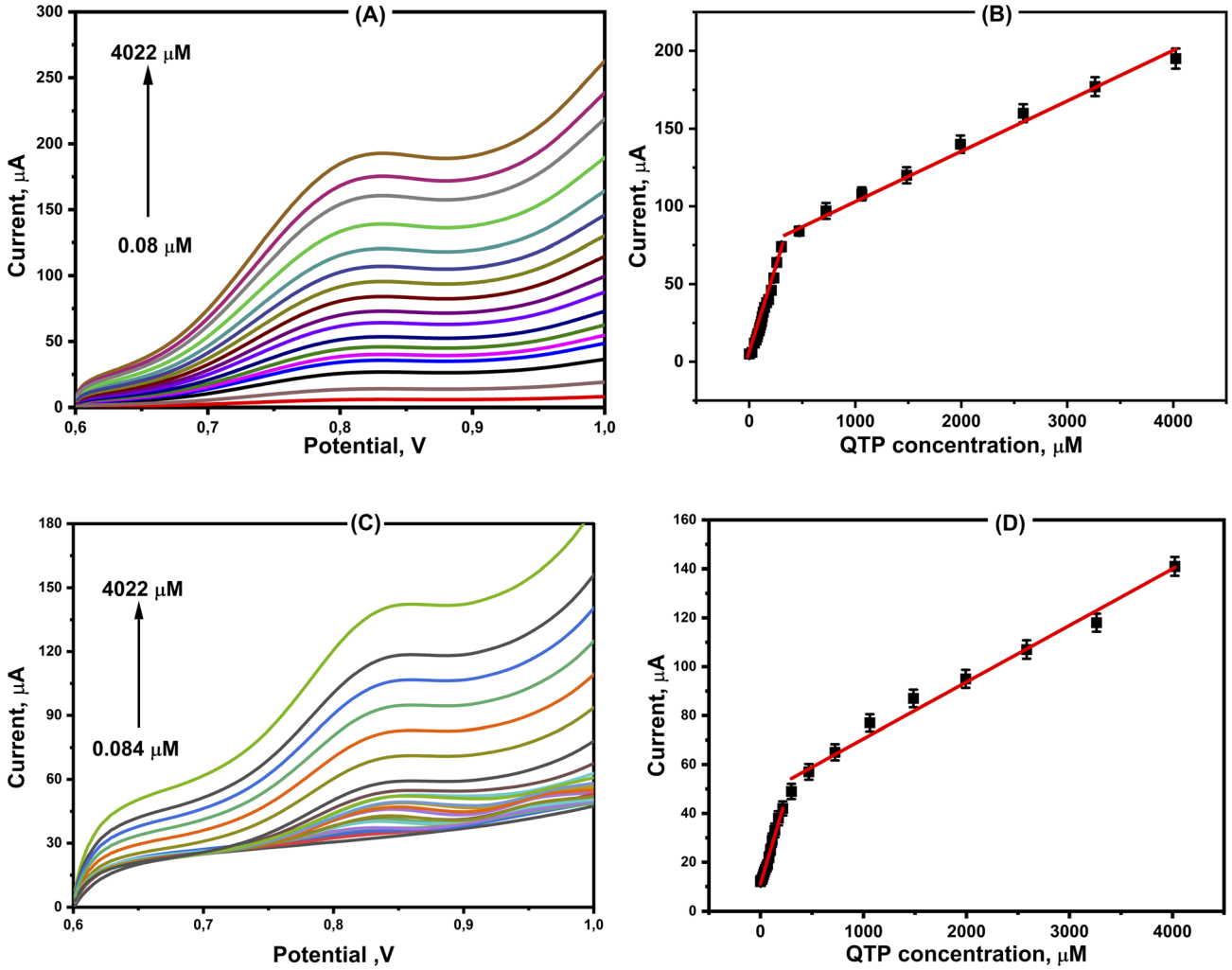

Fig. 7 (A) DPV peaks and (B) linear calibration curve for QTP detection. (C) LSV oxidation peaks and (D) linear calibration curve for the QTP response.

ZrO_2@MWCNTs@GCE sensor to those of previously reported materials (see Tables 1 and 2), it is evident that the proposed electrode exhibits superior sensitivity and a remarkably low detection limit for both CBZ and QTP detection.

It is also important to emphasize that the primary objective of the present study is the electrochemical determination of CBZ and QTP in pharmaceutical formulations. In this context, the active ingredients are often present at relatively high concentrations. Therefore, obtaining wide dynamic linear ranges is essential to enable direct analysis of unknown samples without requiring pre-treatment steps, such as dilution or concentration adjustments. This capability ensures the accurate, rapid, and practical quantification of pharmaceutical analytes under realistic formulation conditions.

Interference study

Given that the optimized electrochemical assay was designed for the quantitative determination of CBZ and QTP in pharmaceutical formulations, evaluating its performance in the presence of potential interfering species is critical. To this end, a range of common pharmaceutical excipients and additives, including silica colloidal anhydrous, ethylcellulose aqueous dispersion, microcrystalline cellulose, polyacrylate, magnesium stearate, sodium carmellose, hypromellose, macroglycerol hydroxystearate, titanium dioxide, povidone, sodium starch glycolate Type A, lactose monohydrate, macrogol, ferric oxide, iron oxide yellow (E172), iron oxide red (E172), and crospovidone, were tested as potential interferents.

The individual electrochemical responses of CBZ and QTP were evaluated using linear sweep voltammetry (LSV) in the absence and presence of these coexisting excipients. As illustrated in Fig. 8, the assay retained rapid, well-defined, and clearly distinguishable voltammetric signals for both CBZ and QTP, demonstrating that the presence of common pharmaceutical additives did not compromise detection. This observation confirms that the ZrO_2@MWCNTs-modified GCE sensor exhibits excellent selectivity, sensitivity, and rapid response characteristics, supporting its suitability for accurate analysis in complex pharmaceutical matrices.

To further assess sensor selectivity, interference studies were conducted using endogenous electroactive species, including

Table 1 Some of the previously reported assays on carbamazepine detection and analysis utilizing different types of nanomaterials for sensor surface modification

Electrode	Method	LOD (μM)	Linear range (μM)	Ref.
Graphite@GCE	CV	4.2	84.6–846	30
MWCNTs@GCE	LSV	0.040	0.13–1.60	31
Fullerene-C_{60}@GCE	DPV	0.0162	0.09–10	32
Gr-AuNP@AuE	LSV	3.03	5.0–0000	33
MI-PEDOT@GCE	SWV	980	—	34
Fe–SnO_2@SPCE	SWV	0.092	0.5–100	35
Au-electrode	CV	0.01	0.1–100	36
ZSM-5/TiO_2@CPE	DPV	1.04	6.0–97	37
NiO/ZnO@GCE	DPV	0.08	5.0–100	38
GO/g-C_3N_4@GCE	AMP	0.0105	0.092–266	39
Au@AgPdNPs-β-CD-IL@GCE	SWV	0.089	0.5–90	40
GR/MWCNTs	DPV	0.233	1.0–60	41
GCE	DPV	4.65 in ethanol 38.1 in water	—	42
TiO_2NPs/Nafion@GCE	DPV	0.054	0.4–12 12–100	43
ERGO-SWNT@GCE	AMP	0.029	0.05–3.0	44
MIPEDOT@GCE	SWV	980	—	34
MIP@CPE	DPV	—	0 to 50	45
AgNPs@SPCE	DPAdSV	0.938		46
[BnMIM]PF_6@CPE	DPV	0.98	7.0–700	47
Ag/TiO_2@CPE	DVP	0.86	2.5–100	48
GCE	DPV	1.8	5.0–600	49
GCE	DPV	0.593	—	50
ZrO_2@MWCNTs@GCE	LSV	0.01	0.08–4022	This work
	DPV		0.08–200	

Table 2 Some of the previously reported assays on quetiapine detection and analysis utilizing different types of nanomaterials for sensor surface modification

Electrode	Method	LOD (μM)	Linear range (μM)	Ref.
GCE	DPV	0.0401	4–200	51
	OSWV	0.133	4–200	
SPAB/GCE	SWAdSV	0.019	0.08–7.5	52
GCE	DPV	0.01	0.02–5	53
GnPs-Naf/GCE	DPV	0.29	1.0–100	54
	DPAdSV	0.022	0.1–10	
GNSs-PDA@SiO_2/rG/GCE	SWV	100	500–3000	55
C–C_3N_4/$Li_2FeMn_3O_8$/IL/CPE	DPV	0.011	0.090–900	56
Pd–Ag/g-C_3N_4/CPE	SWV	1.5	5.2–107	57
ZrO_2@MWCNTs@GCE	LSV	0.025	0.08–4022	This work

ascorbic acid, uric acid, and dopamine, as shown in Fig. 8B and C. Their electrochemical responses were recorded individually and in combination with the target analytes under optimized experimental conditions. The voltammetric profiles revealed well-resolved and distinct three-oxidation peaks, one for each non-targeting specie. Importantly, the introduction of these electroactive compounds alongside CBZ or QTP did not result in peak overlap, alteration of peak potentials, or significant changes in current intensity or peak shape.

The absence of detectable electrochemical interference or redox cross-reactivity indicates that the ZrO_2@MWCNTs-modified sensor possesses strong discrimination capability toward CBZ and QTP, even in the presence of structurally and electrochemically active coexisting species. These results confirm that the electrochemical processes are well resolved and that the sensor maintains reliable signal fidelity under potentially competitive conditions.

Reproducibility and sensor stability

To assess the reproducibility of both the assay and the surface modification process, LSV measurements were conducted using a fixed concentration of 300 μM for CBZ and QTP across multiple freshly prepared ZrO_2@MWCNTs-modified electrodes. As illustrated in Fig. S3A, the oxidation current responses obtained from each electrode were highly consistent, with only a minor relative standard deviation of approximately 2.14%, thereby confirming the excellent reproducibility and uniformity of the sensor fabrication process.

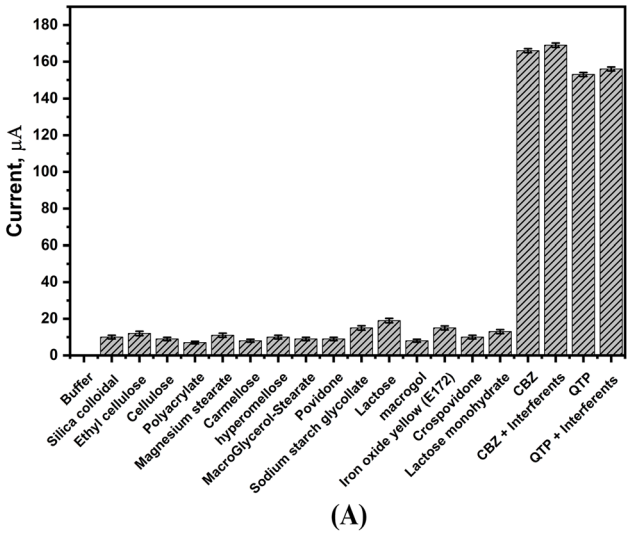

(A)

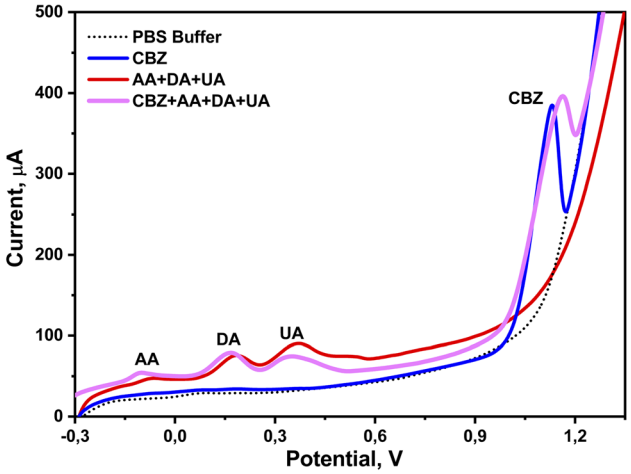

(B)

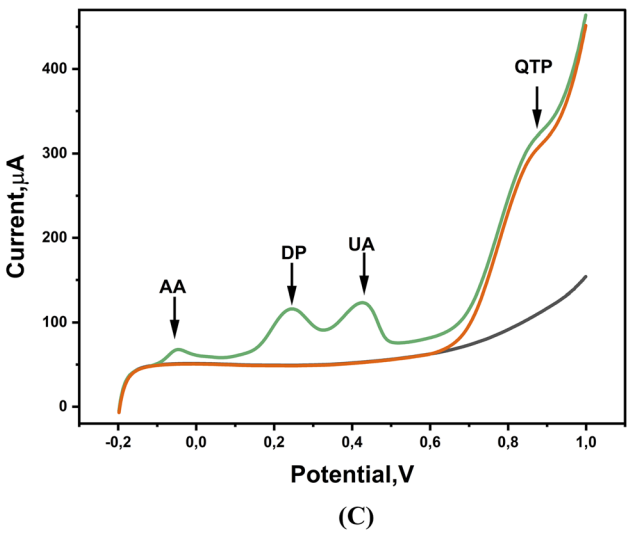

(C)

Fig. 8 (A) Interference study illustrating the voltammetric response of the ZrO_2@MWCNTs-modified electrode in the presence of non-target analytes. (B) Voltammetric detection of multiple electroactive species, including ascorbic acid (AA), dopamine (DA), uric acid (UA), and carbamazepine (CBZ), using the ZrO_2@MWCNTs-modified electrode. (C) Voltammetric detection of multiple electroactive species, including ascorbic acid (AA), dopamine (DA), uric acid (UA), and quetiapine (QTP), using the ZrO_2@MWCNTs-modified electrode.

In addition, the stability and operational durability of the sensor were examined over four weeks following fabrication. As shown in Fig. S3B, the sensor maintained stable electrochemical performance, with only a 5.4% decrease in the oxidation current response over the test period. These results demonstrate that the ZrO_2@MWCNTs-modified electrode possesses outstanding long-term stability and retains its electrochemical activity over extended storage and usage periods.

In addition, the sensor's response time was evaluated by monitoring the voltammetric redox signal immediately following the addition of either CBZ or QTP. The ZrO_2@MWCNTs-modified electrode exhibited a rapid electrochemical response, reflecting fast electron-transfer kinetics at the nanocomposite interface. This swift response indicates that the proposed sensor is well-suited for rapid analytical applications.

Detection of CBZ and QTP in real samples

The developed sensor was essentially designed for practical application in real sample analysis. The optimized electrochemical assay exhibited outstanding sensitivity and selectivity for the detection of CBZ and QTP. Consequently, the quantitative determination of these compounds in pharmaceutical formulations was carried out using the standard addition method. In this evaluation, four raw pharmaceutical drug samples ($n = 4$) were analyzed by the LSV technique, each using individually prepared ZrO_2@MWCNTs-modified electrodes.

The electrochemical responses were recorded, and the corresponding concentrations of CBZ and QTP were calculated from calibration curves established using pure standard solutions. As presented in (Table S5, SI), the recovery values ranged from 99.2% to 100.3%, with relative standard deviations (RSDs) between 1.1% and 3.1%. These results confirm the high precision, accuracy, and analytical reliability of the proposed sensor for real sample quantification.

Overall, the successful detection of CBZ and QTP in pharmaceutical samples underscores the potential of the ZrO_2@MWCNTs-modified sensor for practical implementation in portable analytical devices. Its straightforward fabrication, low cost, and user-friendly operation make it highly suitable for on-site, rapid monitoring of CBZ and QTP without the need for sophisticated instrumentation or extensive technical expertise.

Conclusion

The ZrO_2@MWCNTs-modified electrode (ZrO_2@MWCNTs@GCE) developed in this study provides a highly efficient, stable, and sensitive voltammetric platform for the direct and fast determination of carbamazepine and quetiapine. The fully optimized electrochemical approach exhibited excellent repeatability, reproducibility, and recovery, which was accompanied by remarkably low detection limits. Compared with conventional chromatographic methods, this strategy offers notable advantages in terms of simplicity, rapid response, cost efficiency, and ease of operation.

The synergistic integration of zirconium oxide nanoparticles with multi-walled carbon nanotubes significantly enhanced the electrode's electrocatalytic activity, resulting in substantial signal amplification and pronounced reductions in detection and quantification limits relative to bare and individually modified electrodes. The method's validity was confirmed through the successful quantification of CBZ and QTP in commercial pharmaceutical formulations, demonstrating its analytical precision and practical applicability.

In summary, the ZrO_2@MWCNTs/GCE-based electrochemical sensor constitutes a promising analytical tool for pharmaceutical quality control and therapeutic drug monitoring. Future studies will focus on expanding its application to biological matrices and developing portable or point-of-care diagnostic platforms, thereby broadening its potential for real-world clinical and industrial use.

Author contributions

Dalia A. Aboarayes and Hend S. Magar performed the material synthesis, characterization, and electrochemical measurements, and prepared the original draft of the manuscript. Hassan A. M. Hendawy contributed to the conceptualization and methodology and participated in manuscript review. Rabeay Y. A. Hassan contributed to conceptualization, supervised the project, secured funding, served as principal investigator, and contributed to manuscript revision and final approval.

Conflicts of interest

The authors declare that they have no commercial or financial relationships that could be interpreted as potential conflicts of interest.

Data availability

Data supporting this study are available from the corresponding author upon reasonable request.

Supplementary information (SI) is available. See DOI: https://doi.org/10.1039/d6ra01821a.

Acknowledgements

The authors gratefully acknowledge the financial support provided by the Science, Technology and Innovation Funding Authority (STDF), Cairo, Egypt, for funding the research project "Multiplex Nano-Biosensor for Rapid Breast Cancer Biomarker Detection and Anti-Cancer Agent Screening" (Project ID: 46218, Applied Science, Call 1).

References

1 S. T. Alrashood, in *Profiles of Drug Substances, Excipients and Related Methodology*, ed. H. G. Brittain, Academic Press, 2016, vol. 41, pp. 133–321.
2 W. E. Crill, *Ann. Intern. Med.*, 1973, **79**(6), 844–847.
3 S. D. Waldman, in *Pain Management*, ed. S. D. Waldman and J. I. Bloch, W.B. Saunders, Philadelphia, 2007, pp. 511–517, DOI: 10.1016/B978-0-7216-0334-6.50051-0.
4 S. Pruneanu, F. Pogacean, A. R. Biris, S. Ardelean, V. Canpean, G. Blanita, E. Dervishi and A. S. Biris, *J. Phys. Chem. C*, 2011, **115**, 23387–23394.
5 C. Chen, Y. Wang, S. Ding, C. Hong and Z. Wang, *Microchem. J.*, 2019, **147**, 191–197.
6 R. J. Höpener, A. Kuyer, J. W. A. Meijer and J. Hulsman, *Epilepsia*, 1980, **21**, 341–350.
7 J. S. Maan, T. V. H. Duong and A. Saadabadi, in *StatPearls, StatPearls Publishing Copyright © 2025, StatPearls Publishing LLC., Treasure Island (FL) Ineligible Companies. Disclosure: Truc Vi Duong Declares No Relevant Financial Relationships with Ineligible Companies. Disclosure: Abdolreza Saadabadi Declares No Relevant Financial Relationships with Ineligible Companies*, 2025.
8 L. M. Fuhr, F. Z. Marok, N. Hanke, D. Selzer and T. Lehr, *Pharmaceutics*, 2021, **13**, 270.
9 E. Perucca, O. Dulac, S. Shorvon and T. Tomson, *CNS Drugs*, 2001, **15**, 609–621.
10 R. Kurlan, J. Cummings, R. Raman and L. Thal, *Neurology*, 2007, **68**, 1356–1363.
11 B. Abbas Moussa, M. A. Mahrouse and M. G. Fawzy, *J. Pharm. Biomed. Anal.*, 2019, **163**, 153–161.
12 M. Li, S. Zhang, A. Shi, W. Qi and Y. Liu, *J. Chromatogr., B*, 2017, **1060**, 10–14.
13 V. Pucci, R. Mandrioli, A. Ferranti, S. Furlanetto and M. A. Raggi, *J. Pharmaceut. Biomed. Anal.*, 2003, **32**, 1037–1044.
14 N. Nuchtavorn, J. Leanpolchareanchai, D. Chanton, P. Supapsophon, S. Chongruchiroj, J. Chatmapanrangsee and J. Suksiriworapong, *Pharm. Chem. J.*, 2021, **55**, 845–854.
15 H. S. Magar, B. A. Hemdan, H. R. M. Rashdan and R. Y. A. Hassan, *J. Anal. Test.*, 2024, **8**, 478–492.
16 N. Yousf, E. Ouda, H. S. Magar, R. Y. A. Hassan, S. A. Mansour and E.-S. M. Duraia, *J. Electrochem. Soc.*, 2022, **169**, 047518.
17 R. Singh, R. Gupta, D. Bansal, R. Bhateria and M. Sharma, *ACS Omega*, 2024, **9**, 7336–7356.
18 R. Y. A. Hassan, A. M. Kamel, M. S. Hashem, H. N. A. Hassan and M. A. Abd El-Ghaffar, *J. Solid State Electrochem.*, 2018, **22**, 1817–1823.
19 R. Y. A. Hassan and U. Wollenberger, *Electroanalysis*, 2019, **31**, 1112–1117.
20 H. A. Hussein, A. Kandeil, M. Gomaa and R. Y. A. Hassan, *Microsyst. Nanoeng.*, 2023, **9**, 105.
21 R. Y. A. Hassan and U. Wollenberger, *Anal. Bioanal. Chem.*, 2016, **408**, 579–587.
22 H. S. Magar, A. Shekhar, U. Bilitewski and R. Y. A. Hassan, *Adv. Compos. Hybrid Mater.*, 2025, **8**, 398.
23 E.-S. M. Duraia, B. M. Adebiyi, S. Das, H. S. Magar, G. W. Beall and R. Y. A. Hassan, *Phys. E*, 2024, **159**, 115902.
24 N. Rajab, H. Ibrahim, R. Y. A. Hassan and A. F. A. Youssef, *RSC Adv.*, 2023, **13**, 21259–21270.
25 R. M. Needa, H. Ibrahim, A. F. A. Youssef and R. Y. A. Hassan, *Nanoscale*, 2026, **18**, 4937–4949.

26 H. S. Magar, E.-S. M. Duraia and R. Y. A. Hassan, *Sci. Rep.*, 2025, **15**, 11229.
27 E. Rasouli, M. Abdollahnejad, M. Rahimnejad and H. Ezoji, *J. Indian Chem. Soc.*, 2025, **102**, 102212.
28 R. M. Needa, H. Ibrahim, A. F. A. Youssef and R. Y. A. Hassan, *Nanoscale*, 2026, **18**(9), 4937–4949.
29 R. S. Santos, L. F. Z. Felipe and G. N. Meloni, *ACS Electrochem.*, 2026, **2**, 478–485.
30 S. Atkins, J. Sevilla, M. Blázquez, T. Pineda and J. González-Rodríguez, *Electroanalysis*, 2010, **22**, 2961–2966.
31 A. Veiga, A. Dordio, A. J. Carvalho, D. M. Teixeira and J. G. Teixeira, *Anal. Chim. Acta*, 2010, **674**, 182–189.
32 S. S. Kalanur, S. Jaldappagari and S. Balakrishnan, *Electrochim. Acta*, 2011, **56**, 5295–5301.
33 S. Pruneanu, F. Pogacean, A. Biris, S. Ardelean, V. Canpean, G. Blanita, E. Dervishi and A. Biris, *J. Phys. Chem. C*, 2011, **115**, 23387–23394.
34 A. Hammoud, D. Chhin, D. K. Nguyen and M. Sawan, *Biosens. Bioelectron.*, 2021, **180**, 113089.
35 N. Lavanya, C. Sekar, S. Ficarra, E. Tellone, A. Bonavita, S. G. Leonardi and G. Neri, *Mater. Sci. Eng., C*, 2016, **62**, 53–60.
36 N. Trisovic, B. Božić, S. Petrovic, S. Tadic and M. Avramov-Ivic, *Hem. Ind.*, 2014, **68**, 207–212.
37 S. K. Hassaninejad-Darzi and F. Shajie, *Mater. Sci. Eng., C*, 2018, **91**, 64–77.
38 N. Qambrani, J. A. Buledi, N. H. Khand, A. R. Solangi, S. Ameen, N. S. Jalbani, A. Khatoon, M. A. Taher, F. H. Moghadam, M. Shojaei and F. Karimi, *Chemosphere*, 2022, **303**, 135270.
39 P. Balasubramanian, T. S. T. Balamurugan, S.-M. Chen, T.-W. Chen, M. Ajmal Ali, F. Al-Hemaid and M. Elshikh, *J. Electrochem. Soc.*, 2018, **165**, B160–B166.
40 L. Daneshvar and G. H. Rounaghi, *J. Electrochem. Soc.*, 2017, **164**, B177–B183.
41 L. Daneshvar, G. Rounaghi, Z. E'Shaghi, M. Chamsaz and S. Tarahomi, *J. Mol. Liq.*, 2016, **215**, 316–322.
42 S. Atkins, R. Jiménez Pérez, J. M. Sevilla, M. Blázquez, T. Pineda and J. González-Rodríguez, *Int. J. Electrochem. Sci.*, 2013, **8**, 2056–2068.
43 S. Tarahomi, G. H. Rounaghi, M. Zavar and L. Daneshvar, *J. Electrochem. Soc.*, 2018, **165**, B946–B952.
44 B. Unnikrishnan, V. Mani and S.-M. Chen, *Sens. Actuators, B*, 2012, **173**, 274–280.
45 Aaryashree, A. K. Choudhary and Y. Yoshimi, *Sensors*, 2023, **23**, 3271.
46 M. A. García-García, O. Domínguez-Renedo, M. A. Alonso-Lomillo and J. Arcos, *Sens. Lett.*, 2009, **7**, 586–591.
47 L.-H. Liu, C. Duan and Z.-N. Gao, *J. Serb. Chem. Soc.*, 2012, **77**, 483–496.
48 M. Maashhadizadeh, R. Refahati and E. Amereh, *Anal. Bioanal. Electrochem.*, 2013, **5**, 270–282.
49 S. Kalanur, S. Shankara and S. Jaldappagari, *Anal. Lett.*, 2010, **43**, 618–630.
50 L. Lin, M. Pan, H. Wang, Y. Su and P. Huang, *Med. Chem. Res.*, 2012, **21**, 4389–4394.
51 S. Ozkan, B. Dogan-Topal and B. Uslu, *Microchim. Acta*, 2006, **153**, 27–35.
52 B. Nigović and J. Spajić, *Talanta*, 2011, **86**, 393–399.
53 M. A. El-Shal, *Adv. Pharm. Bull.*, 2013, **3**, 339–344.
54 B. Nigović, A. Mornar and M. Sertić, *Microchim. Acta*, 2016, **183**, 1459.
55 K. Ghaseminasab, N. Aletaha, M. Hasanzadeh, Y. Liu and F. Seidi, *J. Mol. Recognit.*, 2022, **35**, e2977.
56 S. Nazari, M. Shabani-Nooshabadi and N. Ziaie, *Microchem. J.*, 2023, **191**, 108835.
57 Z. Alipour, S. Hassaninejad-Darzi and M. Asadollahi-Baboli, *J. Alloys Compd.*, 2023, **941**, 168958.